

Farhad Javid¹

e-mail: farhad@cim.mcgill.ca

Jorge Angeles

ASME Fellow

e-mail: angeles@cim.mcgill.ca

Centre for Intelligent Machines (CIM) and
Department of Mechanical Engineering,
McGill University,
Montreal, Quebec, H3A 0C3

Damiano Pasini

ASME Member

Department of Mechanical Engineering,
McGill University,
Montreal, Quebec, H3A 0C3
e-mail: damiano.pasini@mcgill.ca

Renzo Cecere

Biosurgery and Design Unit,
Department of Surgery,
McGill University Health Centre,
Montreal, Quebec, H3A 1A1
e-mail: renzo.cecere@muhc.mcgill.ca

Shape Optimization of a Self-deployable Anchor Designed for Percutaneous Mitral Valve Repair

A new percutaneous annuloplasty technique for mitral regurgitation is proposed here. In this technique, inter-related anchors are first inserted around the annulus via a trans-septal catheter. The tethered wire passed through the anchors is then pulled to shrink the annulus and stop regurgitation. The anchors should withstand large deformation, applied during the delivery process, and should recover their original shape after being released inside the tissue. The shape of the anchors is, thus, optimized in an iterative process, to avoid stress concentration by minimizing the weighted rms value of the curvature along the anchor. The weight coefficients in each iteration are defined based on the stress distribution of the anchor obtained in the previous iteration. The procedure finally results in a structurally optimum anchor with a minimum in the maximum von Mises stress. This anchor is fabricated from Nitinol and tested in a cadaveric swine heart.

[DOI: 10.1115/1.4005780]

1 Introduction

Mitral regurgitation (MR) is a valvular heart disease in which the valve does not close completely during the contraction phase and, therefore, blood leaks backward from the left ventricle to the left atrium. If left untreated, MR leads to irreversible heart damage, cardiac arrhythmia and congestive heart failure [1]. Currently, the clinical treatment of MR requires open-heart surgery with cardiopulmonary bypass, which prevents high-risk patients from undergoing the repair. Hence, the motivation to develop alternative procedures such as minimally invasive percutaneous interventions, which would greatly increase the number of potential candidates for repair and significantly decrease the risk associated with conventional surgery.

In the percutaneous annuloplasty technique that is proposed here, interrelated anchors are first inserted around the annulus using a flexible catheter, as shown in Fig. 1. Similar to the purse-string effect, the flexible tethered wire in the anchors is then tightened to reduce the annulus lumen, and hence, stop regurgitation [2,3]. The anchors are individually inserted into the proximal end of the delivery system, outside the body, and fed by means of a push-rod to the needle mounted on the distal end (the catheter tip). The distal end, previously maneuvered to the left atrium, freely rotates and is properly orientated for insertion of the anchor. By fixing the catheter tip to the atrium wall, the needle exits and pierces the tissue. The anchor is then pushed to be released into the annulus and grasp the tissue.

The anchors replace the surgeon's suturing and eliminate the knot-tying process required in open-heart annuloplasty. Until now, three different types of implants have been introduced to replace sutures in percutaneous and minimally invasive operations: barbed sutures, surgical staples, and self-closing clips [4–8]. Barbed sutures are a type of knotless surgical thread supplied with directional projections or barbs along their lengths to anchor the surrounding tissue [9,10]. Surgical staples and self-closing clips are both metallic implants that require special instruments for

their insertion and are mainly developed to replace sutures in endoscopic and laparoscopic operations [11–14]. The high pulling forces required to shrink the mitral valve, the limited accessibility in the percutaneous interventions, and the special geometry of the atrium inner wall prevent the use of currently available implants and call for the design of a new anchor for the percutaneous technique proposed here. The new self-deformable hook-shape implant shown in Fig. 2 is, therefore, proposed for the catheter-based operation. The arms are compressed to be fitted into the catheter lumen during the delivery process and open to grasp the annulus when released into the tissue. The design of this anchor, based on a shape optimization algorithm, is reported in this work.

2 Anchor Design

According to our preliminary experiments conducted on a harvested veal heart [2], the anchor shown in Fig. 2 with the dimensions given in Eq. (1) can resist the wire pull applied to shrink the mitral valve, without tearing the tissue

$$\begin{aligned} r &= 1.2 \text{ mm}, & d &= 0.3 \text{ mm}, & l &= 2.15 \text{ mm}, \\ L &= 6.6 \text{ mm}, & D &= 3 \text{ mm} \end{aligned} \quad (1)$$

Similar to other self-deformable implants, Nitinol is used to build the anchor. Nitinol is an engineering material well-known in the medical industry for its super-elasticity. The Nitinol super-elastic (a.k.a., pseudoelastic) stress-strain relation is shown in Fig. 3, where σ_s^{AS} , σ_f^{AS} , σ_s^{SA} , σ_f^{SA} and ϵ_L are the parameters required in the Nitinol super-elastic constitutive relation [15]. At low stress levels, the stress-strain relation is linear. Upon further loading, the material undergoes a stress-induced martensite transformation—from the austenitic phase to the martensitic phase. During this transformation, large strains are induced in the material, with a plateau section appearing in the stress-strain relation. This relation continues until a second linear path is encountered, with the material completely in the martensite phase. A reverse transformation, from the martensite to the austenite phase, occurs with an offset during the unloading process.

¹Address all correspondence to this author.

Manuscript received February 18, 2011; final manuscript received November 8, 2011; published online March 12, 2012. Assoc. Editor: James Moore.

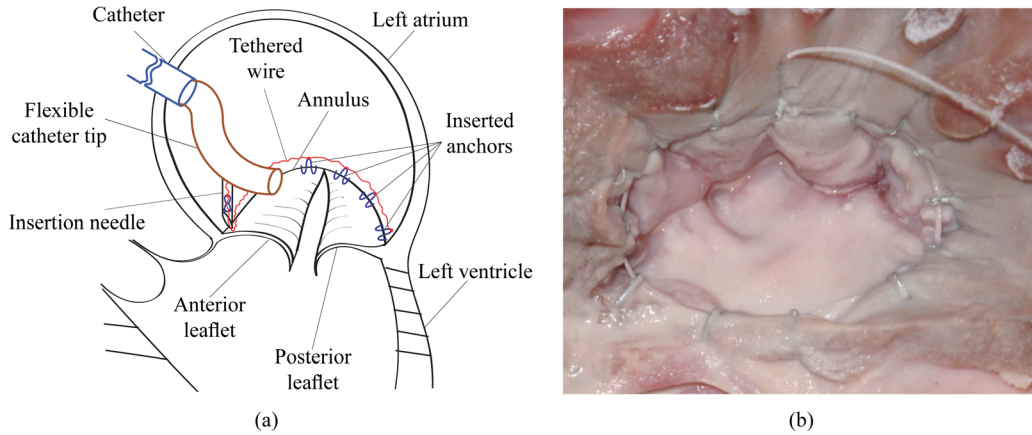


Fig. 1 The percutaneous technique suggested by our research team: (a) schematic illustration; and (b) its implementation on a cadaveric veal heart

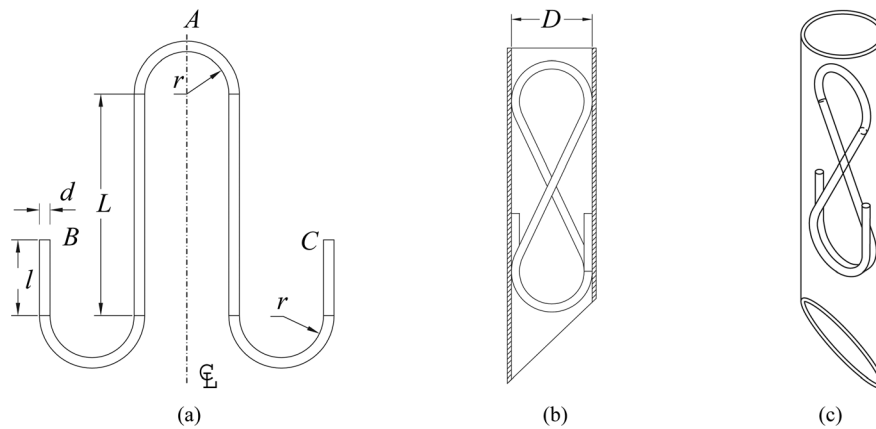


Fig. 2 Schematic shape of the designed anchor: (a) outside the needle; (b) and (c) inside the needle

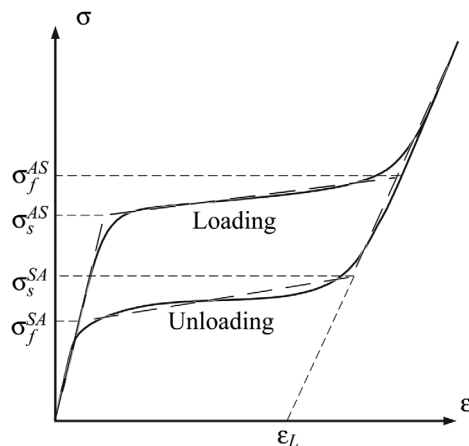


Fig. 3 Super-elastic stress-strain behavior of Nitinol

The finite element analysis (FEA) of the anchor, when inserted inside the 3-mm needle bore, shows that the maximum von Mises stress and strain are, respectively, 514 MPa and 5.45%. Although Nitinol is a super-elastic material, which, by phase transformation, can withstand up to 8% elastic strain, some residual strain remains in the material if it undergoes a higher-than-5% strain. Hence,

shape optimization to avoid stress concentration along the anchor is required to guarantee complete anchor re-opening after insertion into the tissue.

3 Shape Optimization

In mechanical design, geometric primitives such as lines and circles are normally chosen to build mechanical structures. However, when the structure undergoes relatively high deformations, these shapes are not the most suitable ones. Stress concentration, which usually occurs at the blending points of geometric primitives as a result of curvature discontinuity, causes dramatic jumps in the stress values and may lead to the mechanical failure of the structure [16]. Stress concentration can be alleviated by a systematic shape synthesis of the structure mid-curve² to obtain a G^2 -continuous curve—a curve with continuous tangent and curvature—with a curvature distribution of minimum rms value, as proposed in Ref. [17]. Shape optimization for the problem at hand is defined as: *Given two end-points A and B of the curve segment shown in Fig. 4, find a mid-curve Γ that connects the end-points as smoothly as possible with G^2 -continuity under given end conditions.*³

²This is a geometric concept, not to be confused with the *neutral axis* of beams.

³Because of symmetry, only one half of the anchor, part A to B of Fig. 2, is considered.

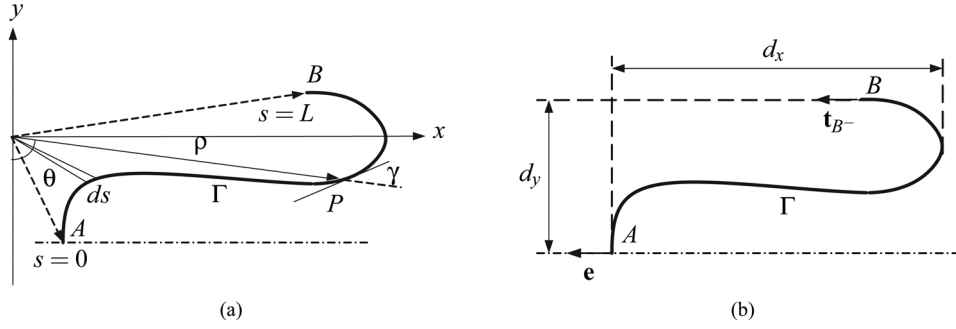


Fig. 4 (a) Schematic G^2 -continuous curve segment, and (b) boundary and dimension constraints

3.1 Problem Formulation. By parameterizing the anchor mid-curve Γ by means of the arc length s along the anchor, the optimization problem can be formulated as

$$J[\Gamma] = \frac{1}{L} \int_A^B \kappa^2 ds \rightarrow \min_{\Gamma(s)} \quad (2)$$

where \sqrt{J} is the rms value of the curvature of the anchor mid-curve Γ , L is the half length of the anchor, A is the anchor mid-point, B is the anchor end point, and ds is the arc length differential along the anchor, starting from 0 at point A (Fig. 4(a)). This problem is subjected to six constraints: four endpoint constraints determine the tangent and the curvature of the anchor mid-curve at points A and B , while the other two determine the length and width of the anchor. At point A , the anchor mid-curve tangent is perpendicular to the pulling direction of the tethered wire, with its curvature being assigned equal to the curvature of the needle bore. At point B , on the contrary, the tangents should be parallel to the pulling direction and the curvature is prescribed as zero. These boundary constraints are formulated as

$$\mathbf{t}_A \perp \mathbf{e}, \quad \mathbf{t}_{B^-} \parallel \mathbf{e}, \quad \kappa_A = \frac{2}{2R-d}, \quad \kappa_{B^-} = 0 \quad (3)$$

where R is the radius of the needle bore and d is the diameter of the anchor wire shown in Fig. 2; \mathbf{t}_A and \mathbf{t}_{B^-} are the unit vectors tangent to the curve at points A and B , pointing in the direction of increasing s , and \mathbf{e} is a unit vector indicating the pulling direction of the wire, as shown in Fig. 4(b). In Eq. (3), B^- indicates that the tangent and the curvature at point B are defined *just before* reaching B , i.e., at $s=L^-$.

In addition to the end point constraints, the dimensions of the anchor are assumed equal to the dimensions of the simple-shape anchor previously analyzed. That is

$$d_x = 2r + d + L, \quad d_y = 3\left(r + \frac{d}{2}\right) \quad (4)$$

with r , L , and d being indicated in Fig. 2, using the dimensions displayed in Eq. (1), while d_x and d_y are shown in Fig. 4(b). The optimization task defined here is a classical problem in the calculus of variations [18]. According to the fundamental lemma of the calculus of variations, Eq. (2) should satisfy a Euler-Lagrange partial differential equation. However, to find a numerical solution, discretization by means of nonparametric cubic splines can be directly applied to reformulate the preceding problem as one of mathematical programming [19]. To this end, $n+2$ supporting points (SP) $\{P_k\}_{k=0}^{n+1}$ are defined along the anchor mid-curve. The k th point has Cartesian coordinates $P_k(x_k, y_k)$. A sketch of the curve segment Γ is shown in Fig. 4(a). Point P denotes a generic point of the curve. In polar coordinates, the spline SPs are defined by $P_k(\rho_k, \theta_k)$, where $P_0=A$ and $P_{n+1}=B$. Moreover, let

$$\Delta\theta = \frac{\theta_B - \theta_A}{n+1} \quad (5)$$

and define $\theta_k = \theta_A + k\Delta\theta$. Furthermore, if we let $\rho(\theta)$ be a cubic polynomial between two consecutive supporting points, $P_k(\rho_k, \theta_k)$ and $P_{k+1}(\rho_{k+1}, \theta_{k+1})$, then we have

$$\rho(\theta) = A_k(\theta - \theta_k)^3 + B_k(\theta - \theta_k)^2 + C_k(\theta - \theta_k) + D_k, \quad \theta_k \leq \theta \leq \theta_{k+1}, \quad 0 \leq k \leq n \quad (6)$$

Three $(n+2)$ -dimensional vectors are defined as

$$\begin{aligned} \boldsymbol{\rho} &= [\rho_0, \rho_1, \dots, \rho_n, \rho_{n+1}]^T \\ \boldsymbol{\rho}' &= [\rho'_0, \rho'_1, \dots, \rho'_n, \rho'_{n+1}]^T \\ \boldsymbol{\rho}'' &= [\rho''_0, \rho''_1, \dots, \rho''_n, \rho''_{n+1}]^T \end{aligned} \quad (7)$$

where ρ'_k and ρ''_k denote the first and second derivatives of the cubic polynomials $\rho(\theta)$ at the k th SP ($\theta = \theta_k$).

The G^2 -continuity imposes linear relationships between $\boldsymbol{\rho}$ and $\boldsymbol{\rho}'$ and between $\boldsymbol{\rho}$ and $\boldsymbol{\rho}''$, namely

$$\mathbf{A}\boldsymbol{\rho} = 6\mathbf{C}\boldsymbol{\rho}' \quad \text{and} \quad \mathbf{P}\boldsymbol{\rho}' = \mathbf{Q}\boldsymbol{\rho}'' \quad (8)$$

with \mathbf{A} , \mathbf{C} , \mathbf{P} , and \mathbf{Q} defined in the Appendix. Furthermore, $\rho_0 = \rho_A$ and $\rho_{n+1} = \rho_B$ are known. Now, let \mathbf{x} be the vector of design variables, defined as

$$\mathbf{x} = [\rho_1, \dots, \rho_n]^T \quad (9)$$

Hence, the discretized shape optimization problem is formulated as

$$z(\mathbf{x}) = \frac{1}{n} \sum_{k=1}^n w_k \kappa_k^2 \rightarrow \min_{\mathbf{x}} \quad (10)$$

where w_k is the weight coefficient, defined at the k th SP, as presently described. Furthermore, the curvature κ_k at point P_k is

$$\kappa_k = \frac{\rho_k^2 + 2(\rho'_k)^2 - \rho_k \rho''_k}{(\rho_k^2 + (\rho'_k)^2)^{3/2}} \quad (11)$$

which can attain positive or negative values. Both are equally penalized by the quadratic objective function $z(\mathbf{x})$ in Eq. (10).

Using the discretized objective function of Eq. (10) and the constraint equations (3) and (4), the problem is formulated as a mathematical program [19]. The orthogonal decomposition algorithm is applied to solve this problem using the ODA package [20].

3.1.1 The Geometrically Optimum Shape. By assuming all the weight coefficients equal to $1/n$ and solving the foregoing

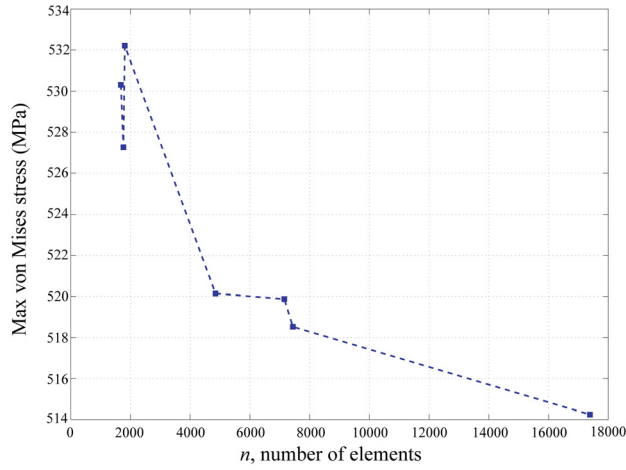


Fig. 5 Maximum von Mises stress of the simple shape anchor versus the number of elements

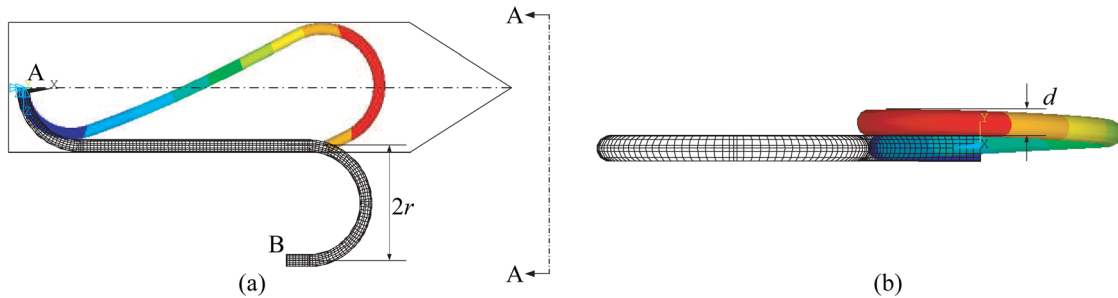


Fig. 6 Applied displacements to the finite element model: (a) in-plane displacement, and (b) out-of-plane displacement

optimization problem, a *geometrically* optimum mid-curve is obtained. This curve is so called because it was obtained with all the weights w_k equal. The G^2 -continuity reduces the stress and strain values along the anchor, with the result of increasing the fatigue life of the structure. However, the stress values can be further reduced, within an iterative procedure. At each iteration, a shape optimization problem similar to the one previously formulated is solved but with nonuniform weights, the anchor thus resulting is structurally analyzed using FEA, with its von Mises stress distribution being used to determine the weight coefficients w_k for the next iteration. The geometrically optimum mid-curve with equal weights can be considered as the first iteration.

3.1.2 The Structurally Optimum Shape. The weights introduced in Eq. (10) are defined at the spline SPs. Each SP defines a cross-section of the anchor. The weight at the k th supporting point is, thus

$$w_k = \frac{\bar{\sigma}_k}{\bar{\sigma}_T} \quad (12)$$

where $\bar{\sigma}_T$ and $\bar{\sigma}_k$ are the rms value of the von Mises stress distribution over the whole anchor and over the k th cross-section, respectively. The strain energy of a mechanical structure is linearly related to the rms value of its stress-deviator tensor. In particular, the rms value of the von Mises stress is proportional to the distortion part of the strain energy. It is known from static failure theory [21] that failure occurs when the distortion component of the strain energy is greater than its yield-stress value. Hence, the weight coefficients indicate how far a cross-section is from failure.

3.2 Finite Element Model (FEM). The geometrical model of the anchor is generated in ANSYS 12.1 from the optimum mid-

Table 1 Material properties of Nitinol

Austenitic module of elasticity (E_A)	70 GPa
Martensitic module of elasticity (E_M)	40 GPa
Poisson's ratio (ν)	0.33
Austenitic yield stress	600 MPa
Martensitic yield stress	120 MPa
Elongation at failure	5 to 10%
Austenitic start temperature (T_s^{AS})	-15°C
Austenitic finish temperature (T_f^{AS})	7°C
Martensitic start temperature (T_s^{SA})	-45°C
Martensitic finish temperature (T_f^{SA})	-24°C
Austenitic start stress (σ_s^{AS})	368 MPa
Austenitic finish stress (σ_f^{AS})	446 MPa
Martensitic start stress (σ_s^{SA})	217 MPa
Martensitic finish stress (σ_f^{SA})	138 MPa
Maximum residual strain (ϵ_L)	5%

curve obtained in each iteration. The anchor is meshed by 20-node hexahedron Solid186 elements using the *sweep mesh* method. A mesh sensitivity analysis is conducted to specify the optimum number of elements for the FEA. The maximum von Mises stress in the simple anchor is plotted versus the number of elements in Fig. 5. Apparently, if the number of elements is selected beyond 15,000, the maximum stress value does not significantly change.

The total number of elements varies between 16,092 and 28,836, the total number of nodes between 69,909 and 125,369, and the aspect ratio of the elements is less than 5 at all iterations. While the model is totally fixed at point A, an in-plane displacement of $2r$ and an out-of-plane displacement of d are applied at point B. The anchor final configuration is shown in Fig. 6.⁴

ANSYS [22] has a built-in *shape memory alloy* material model, proposed by Auricchio [23], for shape memory and super-elastic materials. The parameters of this model were found, tested, and compared with the experimental data for super-elastic Nitinol in Refs. [24,25]. The material properties of the Nitinol wire used to build the anchor are shown in Table 1.

In the FEA, stress and strain are determined at the integration points of the elements and then extrapolated to the nodal locations. These discrete nodal stress values are used to define $\bar{\sigma}_T$ as

$$\bar{\sigma}_T = \sqrt{\frac{1}{m} \sum_{i=1}^m \sigma_i^2} \quad (13)$$

where σ_i is the von Mises stress at the i th node and m is the total number of nodes defined in the FE model. On the contrary, since the FE nodes are independently defined by the FE software, the

⁴To model the anchor in ANSYS, its mid-curve Γ is rotated -90° around the x axis. The XZ plane is, therefore, the plane of Γ in Figs. 6, 8, and 9.

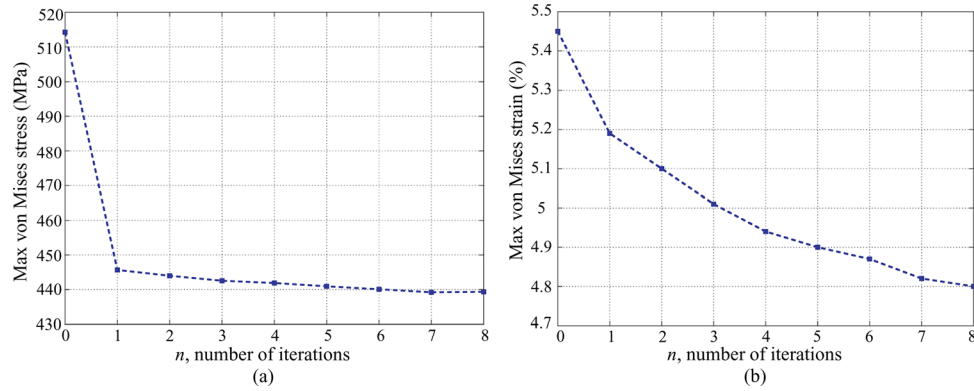


Fig. 7 Evolution of maximum von Mises (a) stress, and (b) strain versus number of iterations

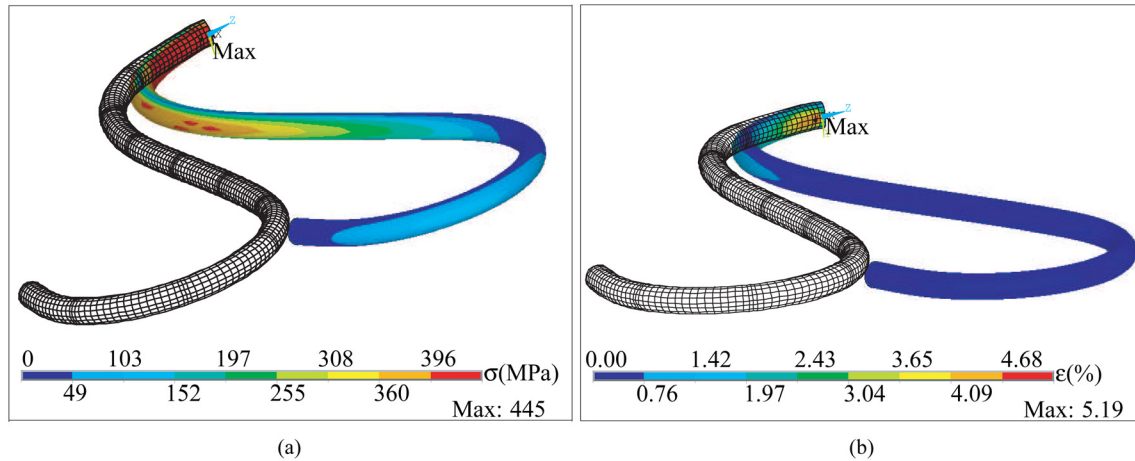


Fig. 8 (a) von Mises stress, and (b) strain distributions of the geometrically optimum anchor

k th cross-section does not necessarily contain any node. In this vein, $\bar{\sigma}_k$ is computed using the μ_k nodes closest to the k th cross-section, as described next

$$\bar{\sigma}_k = \sqrt{\frac{1}{\mu_k} \sum_{i=1}^{\mu_k} \sigma_{ki}^2}, \quad \mu_k = \frac{m}{50} \quad (14)$$

in which σ_{ki} is the von Mises stress at the i th node closest to the k th cross-section and μ_k is 2% of the total FE nodes closest to the k th cross-section. Given the density of the mesh used here, 2% of the nodes are considered sufficient. Increasing μ_k even the weight coefficients in each iteration and reduces the effect of the stress concentration in the structurally optimum mid-curve. The iterative algorithm is stopped when the reduction in the maximum stress value is smaller than 0.1 MPa.

4 Results

Eight iterations were conducted to reach the structurally optimum mid-curve. The evolution of the maximum von Mises stress and strain versus iteration number is shown in Fig. 7. The maximum stress value significantly decreases in the first iteration, the geometrical optimization, and remains almost constant during the next iterations. The maximum strain value, however, shows a more uniform reduction throughout all iterations. The von Mises stress and strain distributions of the geometrically and structurally optimum anchors are shown in Figs. 8 and 9, respectively. Apparently, the maximum von Mises stress is reduced by 13.4% during the geometrical optimization and by 1.3% during the structural

optimization, while the maximum von Mises strain is reduced by 4.8% and 7.5% during the same processes.

5 Discussion

The geometrically and structurally optimum mid-curves are compared in Fig. 10 with the mid-curve of the simple-shape anchor introduced in Sec. 2. The optimum mid-curves are smoother than the simple-shape mid-curve near the axis of symmetry of the anchor (Fig. 10). This shows that point A, located on the symmetry line of the simple-shape anchor shown in Fig. 2, is a critical point with a maximum stress value. Other points with smaller curvature values on the corresponding optimum mid-curve are the connecting points of the geometric primitives used to produce the simple-shape anchor. This confirms that curvature discontinuity in a mechanical structure leads to stress concentration and, hence, it can result in the mechanical failure of the structure.

The geometrically optimum anchor, in comparison with the simple-shape anchor, shows a large reduction in *stress*, with no significant reduction in *strain*. On the contrary, the structurally optimum anchor shows a significant reduction in *strain* while the *stress* reduction is negligible. This can be explained by the Nitinol stress-strain relation shown in Fig. 3. Since the stress state at the critical point⁵ of the simple-shape anchor lies beyond the plateau part of the stress-strain relation, the stress reduction during the geometric iteration, i.e., the first iteration with all weight coefficients equal to unity, is significant. In the iterations that follow,

⁵The critical point is that with maximum von Mises stress and strain.

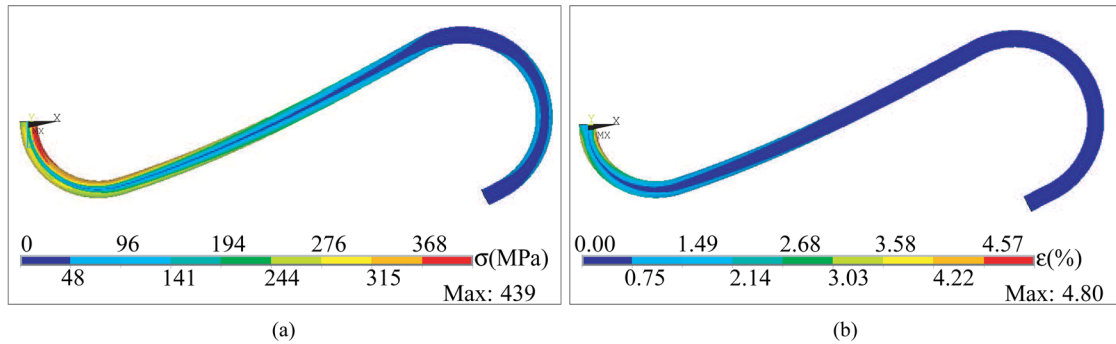


Fig. 9 (a) von Mises stress, and (b) strain distributions of the structurally optimum anchor

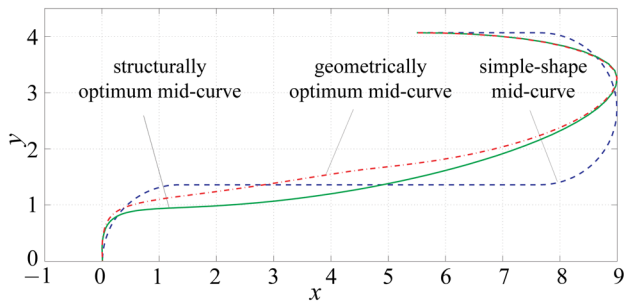


Fig. 10 Geometric and structural optimum mid-curves in comparison with simple shape anchor

the stress state at the critical point lies in the plateau part of the curve, thus resulting in a significant strain reduction.

To experimentally verify the concept, the anchor was prototyped by heating the Nitinol wire to 700°C for 5 min and quenching it with 15°C water. During the heating and quenching process, the wire was kept in the desired optimum shape using a simple fixture. To replicate the percutaneous procedure, as described in Sec. 1, the fabricated anchor was shrunk into a flexible catheterlike tube and, while the tube was inserted into the tissue, the anchor was pushed towards the mitral valve annulus. When released inside the tissue, the anchor arms were deployed; the anchor then firmly grasped the surrounding tissue, as expected. This experiment was performed at a room temperature of 21°C. The anchor is shown in Fig. 11 in its unconstrained state (Fig. 11(a)), inside the tube (Fig. 11(b)), and inside the tissue (Fig. 11(c)).

5.1 Limitations and Future Work. As can be seen in Fig. 3, Auricchio's constitutive relation for super-elastic materials is a

piecewise-linear model which cannot accurately predict the non-linear behavior of Nitinol, especially during the phase transformations. Since the state of the maximum stress point of the anchor is around the martensite transformation, the material model used by ANSYS contains high errors in the FEA. Moreover, the full anchor is not modeled and the boundary conditions of the anchor are simplified in the FEA. Especially, the contact between needle and anchor is not considered, which may increase the stress value at the contact points. More accurate FEA will be conducted in order to validate the results of the simulation runs, in order to precisely predict the stress values along the anchor.

6 Conclusions

The shape optimization of a super-elastic anchor, designed for a percutaneous mitral valve procedure, is reported here. The maximum von Mises stress in the structurally optimum shape was reduced by 14.7% of the corresponding value in the anchor with the original shape; its strain counterpart was reduced by 13.3%. A simple pulling test on the fabricated anchor inserted into the mitral annulus confirms that the anchor can properly grasp the tissue and resist the pulling forces required to reduce the mitral valve lumen. However, the complication of pushing the stressed anchor within a curved catheter along with the fatigue failure of the anchor inserted in a beating heart should be considered before any in vivo test is conducted.

The optimization method can be applied to other surgical implants that work under failure-prone conditions. In particular, the fatigue life of Nitinol implants such as cardiovascular stents, stent-grafts, and the hip and shoulder anchors, which work under cyclic mechanical loading, may be optimized using the shape synthesis algorithm proposed here. It should be mentioned that the Nitinol fatigue fracture, unlike common engineering materials such as steel, is strain-based not stress-based. The oscillating strain amplitude is the main contributor to the Nitinol fatigue [26,27]. The main objective of the optimization process, in this

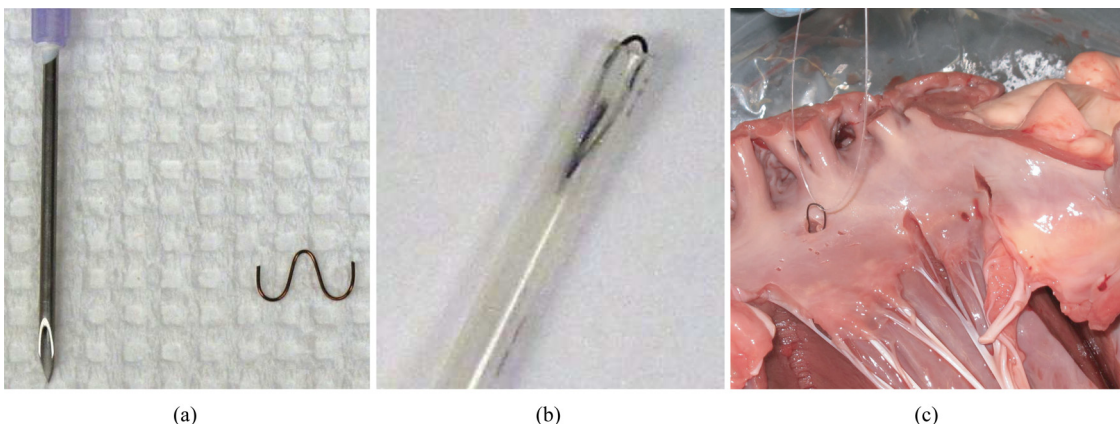


Fig. 11 The anchor (a) fabricated with Nitinol wire to experimentally verify the concept, (b) as inserted into the catheterlike tube, and (c) as released into the mitral annulus

case, is to minimize the amplitude of the oscillating strain during a loading cycle. To this end, two FEAs, one at the zenith and one at the nadir of the loading cycle, should be conducted at each step and the difference of the von Mises strains at each node should be used to define the weight coefficients at the spline SPs.

Acknowledgment

We wish to thank Mr. Toufic Azar, a Ph.D. candidate, for providing us with Nitinol wire and the catheterlike tube and helping us to build and test the anchor. We also thank NSERC, Canada's Natural Sciences and Engineering Research Council, and FQRNT, Quebec's Fonds de Recherche du Québec Nature et Technologies, for their financial support.

Appendix: Continuity Conditions

The linear relationships between vectors ρ , ρ' and ρ'' are expressed in Eq. (8). The constant matrices \mathbf{A} , \mathbf{C} , \mathbf{P} , and \mathbf{Q} in these equations are defined next

$$\mathbf{A} = \Delta\theta \begin{bmatrix} 2 & 1 & 0 & 0 & \dots & 0 & 0 \\ 1 & 4 & 1 & 0 & \dots & 0 & 0 \\ 0 & 1 & 4 & 1 & \dots & 0 & 0 \\ \vdots & \vdots & \vdots & \vdots & \dots & \vdots & \vdots \\ \vdots & \vdots & \vdots & \vdots & \dots & \vdots & \vdots \\ 0 & 0 & \dots & 1 & 4 & 1 & 0 \\ 0 & 0 & 0 & \dots & 1 & 4 & 1 \\ 0 & 0 & 0 & \dots & 0 & 1 & 2 \end{bmatrix} \quad (\text{A1a})$$

$$\mathbf{C} = \frac{1}{\Delta\theta} \begin{bmatrix} c_{11} & 1 & 0 & 0 & \dots & 0 & 0 \\ 1 & 4 & 1 & 0 & \dots & 0 & 0 \\ 0 & 1 & -2 & 1 & \dots & 0 & 0 \\ \vdots & \vdots & \vdots & \vdots & \dots & \vdots & \vdots \\ \vdots & \vdots & \vdots & \vdots & \dots & \vdots & \vdots \\ 0 & 0 & \dots & 1 & -2 & 1 & 0 \\ 0 & 0 & 0 & \dots & 1 & -2 & 1 \\ 0 & 0 & 0 & \dots & 0 & 1 & c_{n''n''} \end{bmatrix} \quad (\text{A1b})$$

in which $n'' = n + 2$ and

$$c_{11} = -1 - \frac{\Delta\theta}{t_A}, \quad c_{n''n''} = -1 + \frac{\Delta\theta}{t_B} \quad (\text{A1c})$$

$$\mathbf{P} = \Delta\theta \begin{bmatrix} 1/\Delta\theta & 0 & 0 & 0 & \dots & 0 & 0 \\ 1 & 4 & 1 & 0 & \dots & 0 & 0 \\ 0 & 1 & 4 & 1 & \dots & 0 & 0 \\ \vdots & \vdots & \vdots & \vdots & \dots & \vdots & \vdots \\ \vdots & \vdots & \vdots & \vdots & \dots & \vdots & \vdots \\ 0 & 0 & \dots & 1 & 4 & 1 & 0 \\ 0 & 0 & 0 & \dots & 1 & 4 & 1 \\ 0 & 0 & 0 & \dots & 0 & 0 & 1/\Delta\theta \end{bmatrix} \quad (\text{A1d})$$

$$\mathbf{Q} = \begin{bmatrix} 1/t_A & 0 & 0 & 0 & \dots & 0 & 0 \\ -3 & 0 & 3 & 0 & \dots & 0 & 0 \\ 0 & -3 & 0 & 3 & \dots & 0 & 0 \\ \vdots & \vdots & \vdots & \vdots & \dots & \vdots & \vdots \\ \vdots & \vdots & \vdots & \vdots & \dots & \vdots & \vdots \\ 0 & 0 & \dots & -3 & 0 & 3 & 0 \\ 0 & 0 & 0 & \dots & -3 & 0 & 3 \\ 0 & 0 & 0 & \dots & 0 & 0 & 1/t_B \end{bmatrix} \quad (\text{A1e})$$

The end-conditions t_A and t_B are given by

$$t_A = \tan \gamma_A, \quad t_B = \tan \gamma_B \quad (\text{A1f})$$

where γ_A and γ_B are the angles between the tangent to the curve and the radius vector at the end-points A and B , as shown in Fig. 4(a).

References

- [1] Yiu, S. F., Enriquez-Sarano, M., Tribouilloy, C., Seward, J. B., and Tajik, A. J., 2000, "Determinants of the Degree of Functional Mitral Regurgitation in Patients with Systolic Left Ventricular Dysfunction: A Quantitative Clinical Study," *Circulation*, **102**(12), pp. 1400–1406.
- [2] Azar, T., Angeles, J., Kovacs, J., and Cecere, R., 2010, "The Mathematical Model of a Procedure for Percutaneous Annuloplasty," *ASME International Design Engineering Technical Conferences and Computers and Information in Engineering Conference*, Vol. 1 of 36th Design Automation Conference, ASME, pp. 1219–1224.
- [3] Javid, F., Angeles, J., Pasini, D., and Cecere, R., 2010, "Optimum Design of an Anchoring System for Percutaneous Mitral Valve Repair," *ASME International Design Engineering Technical Conferences and Computers and Information in Engineering Conference*, Vol. 1 of 36th Design Automation Conference, ASME, pp. 1181–1189.
- [4] Villa, M. T., White, L. E., Alam, M., Yoo, S. S., and Walton, R. L., 2008, "Barbed Sutures: A Review of the Literature," *Plast. Reconstr. Surg.*, **121**(3), pp. 102e–108e.
- [5] Swain, C. P., 1999, "Endoscopic Suturing," *Best Pract. Res. Clin. Gastroenterol.*, **13**(1), pp. 97–108.
- [6] Hill, A. C., Maroney, T. P., and Virmani, R., 2001, "Facilitated Coronary Anastomosis Using a Nitinol U-clip Device: Bovine Model," *J. Thorac. Cardiovasc. Surg.*, **121**(5), pp. 859–870.
- [7] Qadeer, M. A., Dumot, J. A., Vargo, J. J., Lopez, M. R., and Rice, T. W., 2007, "Endoscopic Clips for Closing Esophageal Perforations: Case Report and Pooled Analysis," *Gastrointest. Endosc.*, **66**(3), pp. 605–611.
- [8] Reade, C. C., Bower, C. E., Bailey, B. M., Maziarz, D. M., Masroor, S., Kypson, A. P., Nifong, L. W., and Chitwood, W. R., 2005, "Robotic mitral valve Annuloplasty With Double-Arm Nitinol U-Clips," *Ann. Thorac. Surg.*, **79**(4), pp. 1372–1376.
- [9] Ingle, N. P. and King, M. W., 2010, "Optimizing the Tissue Anchoring Performance of Barbed Sutures in Skin and Tendon Tissues," *J. Biomech.*, **43**(2), pp. 302–309.
- [10] Ingle, N. P., King, M. W., and Zikry, M. A., 2010, "Finite Element Analysis of Barbed Sutures in Skin and Tendon Tissues," *J. Biomech.*, **43**(5), pp. 879–886.
- [11] Burstin, P. P. and Merry, D., 1998, "Endoscopic Stapling Treatment of Pharyngeal Pouch," *Aust. N. Z. J. Surg.*, **68**(7), pp. 532–535.
- [12] Feroli, P., Franzini, A., Messina, G., Tringali, G., and Broggi, G., 2008, "Use of Self-Closing U-Clips for Dural Repair in Mini-Invasive for Herniated Disk," *Acta Neurochir. Suppl. (Wein)*, **150**(10), pp. 1103–1105.
- [13] Guglielminotti, P., Bini, R., Fontana, D., and Leli, R., 2009, "Laparoscopic Repair for Perforated Peptic Ulcers With U-Clip," *World J. Emerg. Surg.*, **4**(28), pp. 1–3.
- [14] Ono, M., Wolf, R. K., Angouras, D., and Schneeberger, E. W., 2002, "Early Experience of Coronary Artery Bypass Grafting With a New Self-Closing Clip Device," *J. Thorac. Cardiovasc. Surg.*, **123**(4), pp. 783–787.
- [15] Auricchio, F., 1996, "Shape-Memory Alloys: Applications, Micromechanics, Macromodelling and Numerical Simulations," PhD thesis, University of California at Berkeley, Berkeley, CA.
- [16] Neuber, L., 1961, "Theory of Notch Stresses: Principles for Exact Calculation of Strength with Reference to Structural Form and Material," U.S. Atomic Energy Commission, Washington, D.C.
- [17] Teng, C. P., Bai, S., and Angeles, J., 2007, "Shape Synthesis in Mechanical Design," *Acta Polytech.*, **47**(6), pp. 56–62.
- [18] Gelfand, I. M. and Fomin, S. V., 2000, *Calculus of Variations*, Dover, Mineola, NY.
- [19] Hillier, F. S. and Lieberman, G. J., 1995, *Introduction to Mathematical Programming*, McGraw-Hill, New York.
- [20] Teng, C. P. and Angeles, J., 2001, "A Sequential-Quadratic-Programming Algorithm Using Orthogonal Decomposition With Gerschgorin Stabilization," *J. Mech. Des.*, **123**(4), pp. 501–509.
- [21] Pook, L. P., 2000, *Linear Elastic Fracture Mechanics for Engineers: Theory and Applications*, WIT, Southampton, Boston, MA.
- [22] ANSYS Inc., 2009, *ANSYS 12.1 Documentations*, Canonsburg, PA.
- [23] Auricchio, F., Taylor, R. L., and Lubliner, J., 1997, "Shape-Memory Alloys: Macromodelling And Numerical Simulations of the Superelastic Behavior," *Comput. Methods Appl. Mech. Eng.*, **146**(4), pp. 281–312.
- [24] Favier, D., Liu, Y., Orgeas, L., Sandel, A., Debove, L., and Comte-Gazac, P., 2006, "Influence of Thermomechanical Processing on the Superelastic Properties of a Ni-rich Nitinol Shape Memory Alloy," *Mater. Sci. Eng., A*, **429**(2), pp. 130–136.
- [25] Wu, W., Qi, M., Liu, X., Yang, D., and Wang, W., 2007, "Delivery and Release of Nitinol Stent in Carotid Artery and Their Interactions: A Finite Element Analysis," *J. Biomech.*, **40**(13), pp. 3034–3040.
- [26] Tolomeo, D., Davidson, S., and Santinoranont, M., 2000, "Cyclic Properties of Superelastic Nitinol: Design Implications," *SMST: Proceedings of the International Conference on Shape Memory and Superelastic Technologies*, pp. 471–476.
- [27] Kugler, C., Matson, D., and Perry, K., 2000, "Non-Zero Mean Fatigue Test Protocol for NiTi," *SMST: Proceedings of the International Conference on Shape Memory and Superelastic Technologies*, pp. 409–417.